Wetting and swelling behaviour of *N*-acetylated thin chitosan coatings in aqueous media

Péter Márton [a], Beáta Szolnoki [b], Norbert Nagy [c], András Deák [c], Dániel Zámbó [c], Gabriella Stefánia Szabó [d,**], Zoltán Hórvölgyi [a,*]

[a] *Budapest University of Technology and Economics, Faculty of Chemical Technology and Biotechnology, Department of Physical Chemistry and Materials Science, Centre for Colloid Chemistry, H-1111 Budapest, Hungary*
[b] *Budapest University of Technology and Economics, Faculty of Chemical Technology and Biotechnology, Department of Organic Chemistry and Technology H-1111 Budapest, Hungary*
[c] *Institute for Technical Physics and Materials Science, Centre for Energy Research, H-1121 Budapest, Hungary*
[d] *Universitatea Babes-Bolyai, Department of Chemistry and chemical engineering of Hungarian Line of study, 11 Arany Janos str., RO-400028, Cluj-Napoca, Romania*

ARTICLE INFO

ABSTRACT

Chitosan nanocoatings (thickness range of 120–540 nm) were produced on glass, zinc and silicon substrates with dip-coating and spin coating techniques to study their pH-dependent wetting and swelling behaviour. The coatings were *N*-acetylated with the methanolic solution of acetic anhydride to increase the degree of acetylation from 36 % to 100 % (according to ATR-FTIR studies). The measured contact angles of Britton–Robinson (BR) buffer solutions (pH 6.0, 7.4 and 9.0) were lower on the acetylated surfaces (*ca.* 50°), than that of their native counterparts (*ca.* 70°) and does not depend on the pH. Contrary, contact angles on the native coating deteriorated 10°-15° with increasing the pH. In addition, for native coatings, the decrease of the contact angles over time also showed a pH dependence: at pH 9.0 the contact angle decreased by 7° in 10 min, while at pH 6.0 it decreased by 13° and at a much faster rate. The constraint swelling of the coatings in BR puffer solutions was studied *in situ* by scanning angle reflectometry. The swelling degree of the native coatings increased significantly with decreasing pH (from 250 % to 500 %) due to the increased number of protonated amino groups, while the swelling degree of acetylated coatings was *ca.* 160 % regardless of the pH. The barrier properties of the coatings were studied by electrochemical tests on zinc substrates. The analysis of polarization curves showed the more permeable character of the acetylated coatings despite the non-polar character of the bulk coating matrix. It can be concluded that in the case of native coatings, 49 % of the absorbed water is in bound form, which does not assist ion transport, while in the case of acetylated coatings, this value is only 33 %.

* Corresponding author. Budapest University of Technology and Economics, Budapest, Hungary.
** Corresponding author. Universitatea Babes-Bolyai, Cluj-Napoca, Romania.
E-mail addresses: marton.peter@vbk.bme.hu (P. Márton), szolnoki.beata@vbk.bme.hu (B. Szolnoki), nagy.norbert@ek-cer.hu (N. Nagy), deak.andras@ek-cer.hu (A. Deák), zambo.daniel@ek-cer.hu (D. Zámbó), gabriella.szabo@ubbcluj.ro (G.S. Szabó), horvolgyi.zoltan@vbk.bme.hu (Z. Hórvölgyi).

1. Introduction

Chitosan is a widely used [1–3] biopolymer, which is made from chitin by partial alkaline deacetylation [4]. It is a copolymer consisting of glucosamine and *N*-acetyl-glucosamine units, the ratio of which is expressed by the degree of acetylation (DA).

Coatings from chitosan can be applied in drug release systems [5], in corrosion protection [6,7], or in membrane technology [8,9], in which the penetration of various species into the coating typically takes place in an aqueous environment. In this case, the fact that the coatings are in a swollen state cannot be ignored, the extent of which (due to the cationic properties of chitosan [10]) is also influenced by the pH of the medium [11].

The swelling of chitosan-based hydrogel layers is mostly monitored by thin layer optical techniques like spectroscopic ellipsometry [12,13] or quartz crystal microbalance [14,15] for nanocoatings. These studies deal with the pH dependence of the swelling, but the effect of DA has been poorly investigated.

In our previous paper [16] the permeability and barrier properties of chitosan nanolayers were investigated as a function of their DA. The *N*-acetylation of the layers was performed using acetic anhydride dissolved in methanol. It was found that DA significantly affects the surface properties of the coatings and their permeability to cationic species. Despite the widespread use of acetylation to create water repellency [17], *N*-acetylation increased the wettability of the coating and reduced its barrier properties. This motivated us to give insights into the interaction of the bulk material of the *N*-acetylated layer with water. Hence, in this study, the swelling characteristics of a native and a highly N-acetylated chitosan nanocoating were investigated as a function of pH by *in situ* scanning angle reflectometry (SAR [18–20]) in aqueous media and the effect of pH and DA are tested.

The thin layer optics, however can only provide reliable information about the swelling if only the thickness of the layer increases during the process (constraint swelling [21,22]) due to the constraint imposed by the attachment to the substrate. The phenomenon of constrained swelling was verified by two independent methods in this work: by measuring the lateral movement of nanoparticles mixed into the coating that is well known in the literature [23] and by the effective medium approximation which has not been used earlier. For comparison, the wetting kinetics of the not modified and the highly *N*-acetylated nanolayers were also studied with aqueous solutions of different pH. In addition, we also performed electrochemical tests, based on the results of which we obtained information about the volume of water channels important for ion transport in the swollen layers. The results can be utilized in controlled drug delivery and in membrane technology processes.

2. Experimental section

2.1. Reagents

All chemicals were used as received without any further purification. Methanol (99.9 % a.r.), isopropyl alcohol (99.7 %, f.a.) and acetic anhydride (f.a.), were provided by Reanal (Hungary), acetic acid (99.8 % f. a.) by Lachner (Czech Republic), and hydrochloric acid (37 % f.a.) and sulfuric acid (96 %, f.a.) by Carlo Erba (Italy). Chitosan (Medium molecular weight: 200,000–300,000 Da, Degree of deacetylation: 75–85 %), phosphoric acid (85 %, f.a.) and boric acid (99.5 % f.a.) were purchased from Merck (Germany), NaOH from Fischer Chemical (USA) and Na_2SO_4 (97 %, f.a.) from Lachema (Czech Republic). Water was purified by a Milli-Q system (Millipore Simplicity 185) and had a specific electrical resistance of 18.2 MΩcm (ultrapure water).

2.2. Sample preparation

2.2.1. Coatings preparation

For the sake of different tests, we produced the coatings on different substrates. The UV–Vis spectroscopy and microscopy required a transparent substrate, so glass were used and most of the further tests were performed on these samples (IR-spectroscopy, AFM and contact angle measurements). Zinc was used for the electrochemical measurements, because in this case a conductive substrate was necessary so that the sample could be used as an electrode. SAR measurements required a highly reflective substrate without backside reflection, so silicon was used, but it was not possible to create the coating for this surface with dip-coating (due to the low polarity of the surface), so spin-coating technique was used. SEM and AFM measurements were also performed on the coatings applied to silicon to validate their thickness and get information about the surface morphology. Before coating preparation, the glass substrates (soda-lime glass microscope slides, Menzel-Gläser, Germany) were washed with 5 % (w/w) aqueous detergent solution, 10 % sulfuric acid solution, isopropyl alcohol and ultrapure water. The Zn plates (Bronzker Bt., Hungary) were prepared by wet grounding on SiC papers (P80 to P2500 particle size) and then polishing by a diamond suspension (3 μm). After the polishing, the substrates were cleaned in ethanol, isopropyl alcohol, and ultrapure water. Before the coating deposition they were immersed in aqueous solution of hydrochloric acid (0.1 M) to clean any remaining zinc-oxide from the surface [16,24]. The silicon substrates (Double Side Polished, 100, Siegert Wafer GmbH, Germany) were cleaned with isopropyl alcohol and ultrapure water, and then plasma treated for 5 min with a Smart-Plasma 10 laboratory plasma system (Plasma Technology GmbH, generator: 40–100 kHz, 300W) for improving the wettability of the surface by the polymer solution. The power was set to 50 % (150 W) and the pressure was 15 Pa.

The 1 % chitosan solution was made by preparing 49.5 mL 1 % (v/v) acetic acid solution from 500 μL 98 % acetic acid and 49.0 g ultrapure water and dissolving 0.5 g chitosan powder in it. The 1.5 % solution was prepared the same way from 0.75 g chitosan, 500 μL acetic acid and 48.75 g ultrapure water. The solutions were stirred for 24 h, then centrifuged with a HERMLE Z36 HK device at 4000 rpm for 30 min to remove the not soluble particles. The coating deposition onto the glass and zinc substrates was performed at room temperature from the 1 % chitosan solution with a dip coater made by Plósz Mérnökiroda Kft., Hungary. The withdrawal speed was of

5 cm/min. Onto the silicon substrates the nanolayer was formed by spin-coating (SCS 6808 Spin Coater, using spinning speed of 9000 rpm) from the 1.5 % chitosan solution (in that case the thickness of the resulted coatings will be similar to that of the dip coated ones). After one dip, the samples were dried overnight.

2.2.2. Chemical modification of the coatings

Some of the prepared coatings were N-acetylated using acetic anhydride dissolved in methanol with the method reported by Choi et al. [25]. In the case of the coatings on glass and zinc substrates, three coatings were immersed into 25 mL methanolic solution and agitated for 24 h on a Heidolph Rotamax 120 laboratory shaker. The concentration of acetic anhydride was 13.33 mM. In the case of the coatings on silicon substrates, three samples were immersed in 5 mL reagent solution with a concentration of 3 mM. In all cases the amount of acetic anhydride was 7.5 molar equivalent for the amount of polymer in one sample (calculated from layer thickness, surface area and number of samples). The chemically modified coatings were cleaned with methanol and dried at 22 °C for 20 min. We introduce an abbreviation from the native chitosan samples (CS) and the N-acetylated chitosan samples (A-CS).

2.3. Examination of surface properties

2.3.1. AFM measurements: surface morphology

The AFM images on the samples deposited onto silicon substrate were recorded with an AIST-NT SmartSPM 1000 AFM device in tapping mode. For the measurements a PPP-NCHR-20 needle (nominal radius <20 nm, made by NanoSensors) was used. The height and phase image of the samples were recorded in a range of 2×2 and 20×20 μm. The data evaluation was carried out using the Gwyddion software [26].

2.3.2. Wettability measurements

Water and buffer solution contact angles were measured on the CS and A-CS coatings deposited on glass substrates, to study the chemical structure of the surfaces and the effect of pH on that [27]. Measurements were carried out with a Drop Shape Analysis System (DSA30, Krüss GmbH). Advancing contact angles were measured at 25 °C and at least 80 % humidity by the sessile drop method. The data was recorded within the first 20 s after the 10 μL droplet formation. Receding contact angles were measured after removing 5 μL liquid from the droplet. The difference of the advancing and receding angles were called contact angle hysteresis. The advancing contact angles were also recorded for 20 min after dropping the liquid (data were measured in every 20 s). The measurements were made with Britton–Robinson (BR) buffer solutions (pH 6.0, 7.4 and 9.0), the same fluids as those used in the swelling experiments. Under these conditions, an important pH value in biological systems (7.4) and two extreme values can be examined (at pH 6.0 chitosan is fully protonated, while at pH 9.0 it is completely deprotonated). The average values were calculated from the contact angles of at least four droplets (n = 8).

2.4. Examination of bulk properties

2.4.1. UV–visible spectroscopy studies

The thickness and refractive index of the layers (on glass) were calculated by fitting a thin-layer optical model the transmittance spectra (Hild method [28]). The spectra were recorded with 10 nm/s measuring speed, and 1 nm resolution from 350 to 1100 nm by an Analytik Jena Specord 200 UV–Vis spectrophotometer. The thickness and refractive index were calculated from the fitted values of twelve replicate samples (n = 12).

2.4.2. FTIR spectroscopic studies

The FT-IR spectra of the coatings on glass substrates were recorded in ATR mode using a Bruker Tensor 37 FT-IR spectrometer, equipped with deuterated triglycine sulfate (DTGS) detector. The wavenumber range was 4000-650 cm^{-1} and the resolution was 4 cm^{-1}. The baseline-correction of the spectra was carried out with the software of the spectrometer (OPUS 5.5). The degree of acetylation (DA) of the coatings was calculated with the method reported by Domszy and Roberts, using the following equation [29]:

$$DA[\%] = \left(\frac{A_{1655}}{A_{3450} \bullet 1.33} \right) \bullet 100 \tag{1}$$

Where A_{1655} and A_{3450} were the absorbances at 1655 cm^{-1} (peak of the amide group) and 3450 cm^{-1} (peak of the OH group) respectively, and 1.33 represents the ratio of these two absorbances for fully N-acetylated chitosan. The DA values were calculated from the FTIR spectra of six replicate samples (n = 6).

2.4.3. Scanning-angle reflectometry studies of dry and swollen coatings

The reflectance curves of the silicon supported coatings were recorded by a scanning angle-reflectometer made by Plósz Mérnökiroda Kft., Hungary equipped with a Thorlabs HNL05L 15 mW He–Ne laser ($\lambda = 623.8$ nm), and a Thorlabs S120C silicon photodiode detector. The reflectance was measured in the incidence range of 60°–80° for the bare silicon substrate, and in the incidence range of 45°–65° in the case of the dry CS and A-CS coatings with 0.01° resolution. The thickness and effective refractive index of the coatings were determined by fitting a theoretical reflectance function [30] to the measured data of twelve replicate samples (n = 12).

For the swelling experiments, the measurements were carried out in a transparent cylindrical liquid chamber manufactured by Plósz Mérnökiroda Kft., Hungary. For the measurement the CS or A-CS sample was placed in the chamber, and it was filled with the buffer solution or ultrapure water. Several reflectance curves were recorded 1, 10, 20, 30, 60, 120 and 180 min after the filling, in the incidence range of 60°–80° with the same speed and resolution as before. An additional curve were recorded for the bare silicon substrate in the filled liquid chamber with the same parameters for calibration. The refractive indices used in the optical model for the ultrapure water and the buffer solutions were 1.332 and 1.334 respectively, measured with a Kyoto-kem RA-120 refractometer. The values were calculated from the reflectance curves of three replicate samples (n = 3).

The buffer solution for the experiments was a Britton–Robinson buffer, which was made from an acidic solution containing 0.04 M acetic acid, 0.04 M phosphoric acid, and 0.04 M boric acid. The required pH was achieved by adding the basic component (0.2 M NaOH) to the mixture until the desired pH was reached (Checked with a Mettler Toledo InLab Micro glass combined electrode connected to a Sartorius PB-11 pH meter).

2.4.4. Optical microscopic measurements

To study the phenomenon of constrained swelling, the lateral displacement of nanoparticles mixed in the (glass supported) coating were measured in a dry and swollen state [22]. The change in the distance of selected pairs of particles was determined from dark field images taken with an Olympus BX51 microscope. For detailed explanation, see Appendix A.

2.4.5. Electron microscopic measurements

To validate the thickness results obtained from the scanning angle reflectometric measurements, cross-section electron microscopic images were made of a CS and an A-CS sample (on silicon substrate) with a Zeiss Leo 1540XB FE-SEM device. The samples were flash-frozen in liquid nitrogen and broken. The images were taken at 5 kV at different magnifications. The layer thicknesses were determined from the recordings with ten parallel measurements using the ImageJ software [31].
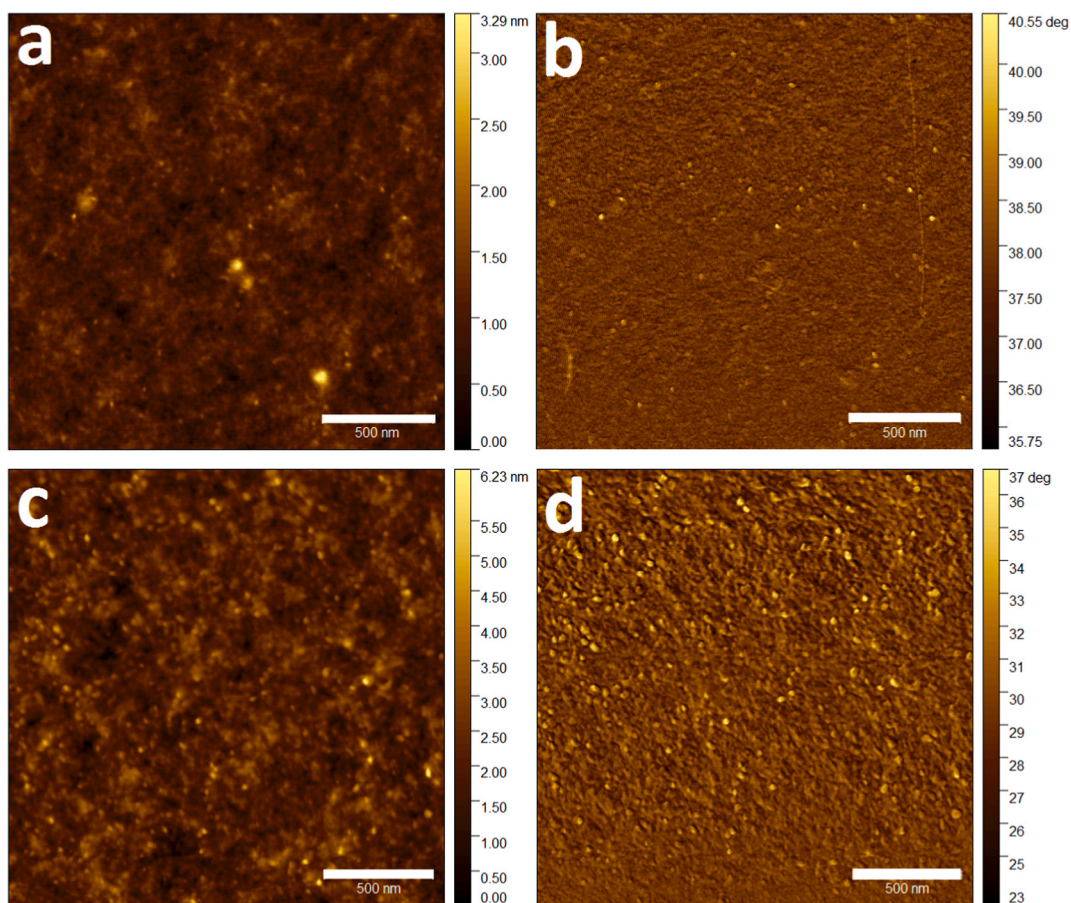

Fig. 1. Recorded height (a, c) and phase (b, d) images for silicon-supported CS coatings (top) and A-CS coatings (bottom). The scale bar is 500 nm in all cases. (For interpretation of the references to colour in this figure legend, the reader is referred to the Web version of this article.)

2.4.6. Electrochemical measurements

Coatings were deposited on Zn substrates to study their permeability in electrochemical tests [7]. DC and AC measurements can be used to evaluate the layers proneness to electrolyte species transport. The result of potentiodymic polarization in low and high potential range are the polarization curves from which the polarization resistance (Rp) and corrosion current density (i$_{corr}$) can be obtained [32]. The linear and semi-logarithmic polarization measurements were carried out in the range of OCP±20 mV and OCP±200 mV vs Ag/AgC,KCl$_{sat}$. They were recorded with a scanning speed of 0.166 mV/s. This reflects the oxidation rate of the metal due to the interaction with aggressive species reached its surface, and characterizes the permeability of the barrier layer by an indirect way. Electrochemical impedance spectroscopy (EIS) is an AC method utilized to obtain information about the behaviour of the coated system. To perform EIS tests, 10 mV amplitude sinusoidal potential signal at open circuit potential (OCP) was applied in 10 mHz-100kHz frequency range. Electrochemical measurements were performed in an undivided three-electrode cell with a PARSTAT 2273 potentiostat. The bare Zn and the coated samples, with 2 cm^2 area [24] represented the working electrode. As reference electrode Ag/AgCl/KCl$_{sat}$ was used and as counter electrode a Pt wire. The electrolyte was 0.2 g/L Na$_2$SO$_4$ which was kept at a constant pH (7.4) with Britton–Robinson buffer solution. Each measurement started with the open circuit potential (OCP) determination (1h) which was followed the EIS and polarization measurements.

2.5. Statistical analysis

Mean with standard deviation and ANOVA test (with a significance level of $p < 0.05$) were used for the statistical analysis using OriginPro 8.6 software (OriginLab Corporation, Northampton, MA, USA). Significant differences in the tables and figures are marked with lowercase letters, where the different letters mean significantly different data points.

3. Results and discussion

3.1. Surface properties of the prepared coatings

When a solvent molecule penetrates into the coating, the interfacial region (or the surface) is the first barrier. Hence, the chemical composition and morphology of this region can greatly affect the wetting and swelling properties. The morphology of the surfaces was studied by atomic force microscopy, while contact angle measurements with buffer solutions provided information about the polarity of surface functional groups.

3.1.1. AFM-studies

The recorded AFM images are shown in Fig. 1, where the height (Fig. 1a and c) and phase (Fig. 1b and d) images of the CS and A-CS coatings on silicone substrate are summarized. The height image shows the height of the measured surface (the distance perpendicular to the substrate plane), while the phase image is related to the interactions of the surface (areas with stronger interaction are brighter). Based on the images, it can be concluded that the surfaces of the two coatings are quite similar. Both are rather smooth and flat, as the difference in the height of the z-scale is only 3 and 6 nm in the case of the CS and A-CS coatings respectively. This smoothness can also be seen from the surface roughness factors, which are 1.000 and 1.002 for the CS and A-CS coatings (determined on 20 × 20 μm^2 areas). Although there is an observable morphological difference between the two kinds of coatings, this is largely due to the fact that the z-scale magnifies surface irregularities, so it can be concluded that the chemical reaction does not have a significant effect on the surface morphology. The results are very similar to those measured on the coatings we previously applied to glass substrate [16], and it can be concluded that the reaction took place evenly and drying did not cause the wrinkling of the coatings.

3.1.2. Contact angles

The advancing and receding contact angles were measured on CS and A-CS coatings with Britton–Robinson (BR) buffer solutions of pH 6.0, 7.4 and 9.0 (Table 1). The resultant contact angle hysteresis values are also shown here. As can be seen, the contact angles are significantly lower for the A-CS coatings, which assumes that in some cases the short-chain and relatively polar acyl group cannot render hydrophobic the coating, and in addition, the more polar OH groups remain intact in the reaction (see section 3.2.2). This

Table 1

Results of the contact angle measurements for all the studied coatings and measuring liquids. (Θ_A: advancing contact angle - measured immediately after dropping, Θ_R: receding contact angle, H_Θ: contact angle hysteresis, Θ_0 Θ_∞ and t_k are the parameters of Eq. (2) and $\Delta\Theta$ is the difference of Θ_0 and Θ_∞). (Mean ± standard deviation, n = 6, significant differences in each individual column are denoted by superscripts a-d, $p < 0.05$).

Sample	Measuring liquid	Measured values			Fitted values (Eq. (2))			
		Θ_A [°]	Θ_R [°]	H_Θ [°]	Θ_0 [°]	Θ_∞ [°]	$\Delta\Theta$ [°]	t_k [s]
Glass/CS	**BR pH 6.0**	70±3[a]	36±2[b]	34±1[a]	68±2[b]	55±1[c]	13±3[a]	43 ± 13[c]
	BR, pH 7.4	72±3[a]	40±2[a]	32±1[a]	70±0[b]	60±0[b]	10±0[a]	103±6[a]
	BR, pH 9.0	73±3[a]	39±3[a]	34±1[a]	73±2[a]	67±3[a]	7±2[b]	102±8[ab]
Glass/A-CS	**BR, pH 6.0**	51±2[b]	25±2[c]	26±2[b]	50±1[c]	45±1[d]	5±0[b]	81±9[b]
	BR, pH 7.4	48±3[b]	24±3[c]	24±3[b]	47±1[d]	43±1[d]	3±1[bc]	117±8[a]
	BR, pH 9.0	48±4[b]	22±3[c]	26±2[b]	48±1[cd]	43±1[d]	5±0[b]	113±7[a]

finding is in good agreement with our previously measured data, and can be explained by the reorganization of the functional groups at the surface, which occurs during the *N*-acetylation reaction in methanolic medium and is then fixed by the rapid evaporation of the solvent [16,33]. It should be noted that the measured contact angle values at the acetylated surfaces do not show pH dependence at all (Fig. 2 and Table 2.) which confirms the presence of the *N*-acetylated groups at the surface.

The advancing contact angles (Fig. 2.) show a significant deterioration in the investigated time (*t*) range (20 min). An exponential decay function [13] were fitted to the contact angles in the first 500 s for a deeper analysis of data. This is the range, where the evaporation of the droplet can be safely neglected on contact angles. The equation of the fitted function is the following:

$$\Theta_A(t) = \Theta_\infty + (\Theta_0 - \Theta_\infty)e^{-t/t_k} \tag{2}$$

where Θ_A is the advancing (measurable) contact angle in time, Θ_0 is the contact angle extrapolated to time zero in the process, Θ_∞ is the stationary value of the contact angle, and t_k is a constant characterizing the rate of decrease. The R^2 value was above 0.96 in all cases, which shows that the empirical model is suitable for the fitting. The values of the fitted parameters are also shown in Table 1 for all coatings and buffer solutions.

One can see from the table, that the Θ_0 values do not differ significantly from the Θ_A values measured on the same sample (n = 6, p < 0.05) within 10 s after the drop formation. This shows that the contact angle values that can be determined this early in time, adequately characterize the initial polarity of the air-dry coatings.

From the results in Table 1 it can be concluded that the surface groups of the CS layer are more mobile in the measuring liquid-solid interfacial layer than those of the A-CS ones, especially at lower pH values (due to the swelling of the layer underneath the droplet, see the swelling results later). This is reflected in a significant decrease of the water contact angles over time and, also, in the lower values of the t_k constant.

In the case of the CS coatings, the stationary contact angles become smaller (Table 1.) at lower pH of the measuring liquid due to the increased number of protonated amino groups at the interface. The larger amount of protonated amino groups at lower pH creates a more polar (hydrophilic) surface that facilitates the penetration of water molecules into the coating and the reorientation of functional groups with their polar part toward the water phase. These processes result in a larger and faster decrease of contact angles (see the lowest t_k value for the CS sample at pH 6.0). The stationary contact angles (or the values measured during the decrease) for the A-CS samples do not show significant pH dependence due to the lack of free amino groups at the surface. Additionally, the more crystalline structure of the A-CS coatings [34] does not favor the reorganization of the polymer chains even at the surface.

3.2. Bulk properties: results

Once the species have passed through the interfacial layer, the properties of the bulk phase (such as polarity, chemical composition and intermolecular interactions) become the determining factors. The bulk properties of the coatings were analyzed using IR and UV–Vis spectroscopy, while the swelling characteristics of the coatings were studied in *in situ* experiments using SAR.

3.2.1. Thickness and refractive index of coatings: UV–Vis spectroscopy and SAR investigations

It was visible that all coatings on all substrates were contiguous and homogenous. The thickness and refractive index of coatings were measured with thin layer optical analysis. For the dip-coated layers on glass substrate, UV–Vis spectroscopic measurements were used. The transmittance spectra for the chitosan layers and the bare glass substrate are shown in Fig. 3a. The average thickness and refractive index of the Glass/CS coatings were 389 ± 9 nm and 1.540 ± 0.001 (n = 12), respectively, while these data for the Glass/A-CS samples were 539 ± 10 nm and 1.517 ± 0.001 (n = 12). That means an average increase in layer thickness of 38 ± 2 %.
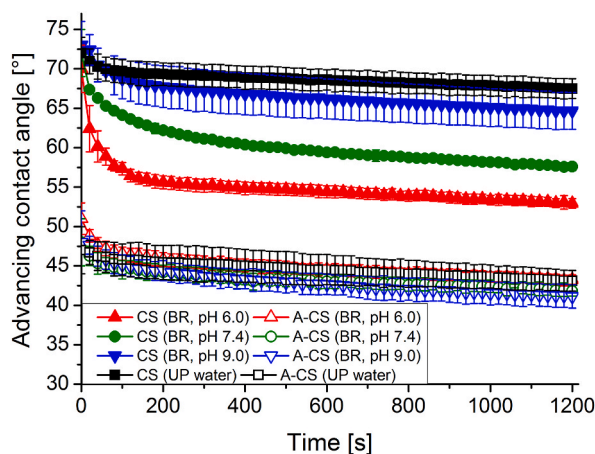

Fig. 2. Advancing contact angles in time for coatings deposited on glass substrate with droplets of different liquids (BR means Britton–Robinson buffer solution with a given pH). (Mean $\pm$ standard deviation, n = 4).

Table 2

Potentiodynamic parameters of bare and CS, A-CS coated Zn, in 0.2 g/L Na$_2$SO$_4$ aqueous solution with pH = 7.4 (*OCP*: open circuit potential after 60 min, *E$_{corr}$*: corrosion potential, *R$_p$*: polarization resistance, *P*: pseudo-porosity, *i$_{corr}$*: corrosion current density, *b$_c$* and *b$_a$*: cathodic and anodic Tafel-slopes, *IE*: inhibition efficiency) Data related to the barrier properties ("permeability") of the coatings are marked in bold.

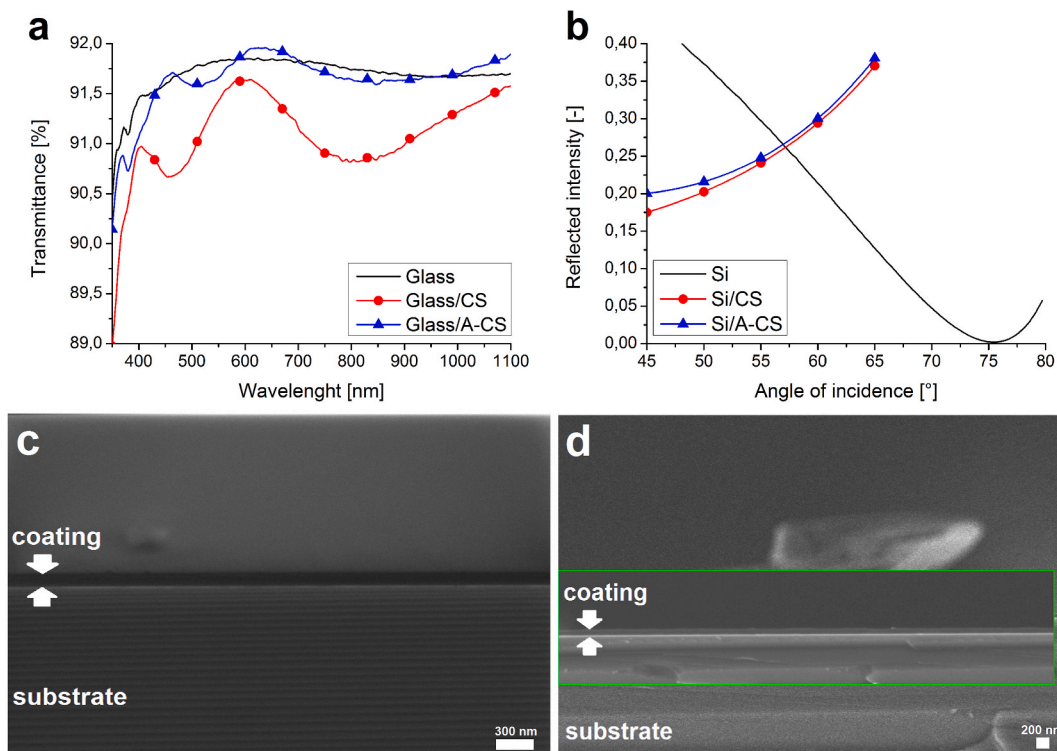| Sample	OCP [V]	Linear polarization			Tafel extrapolation of semi-logarithmic polarization				
		E$_{corr}$ [V]	R$_p$ [Ω]	P [%]	i$_{corr}$ [A/cm^2]	E$_{corr}$ [V]	b$_c$ [V/dec]	b$_a$ [V/dec]	IE [%]
Zn	−0.985	−1.006	1452	**-**	**29.54**	−1.025	0.348	0.140	**-**
Zn/CS	−0.969	−0.974	3420	**25.1**	**7.49**	−0.982	0.211	0.257	**74.6**
Zn/A-CS	−1.053	−1.058	1994	**30.9**	**21.36**	−1.104	0.136	0.252	**38.3**

Fig. 3. Transmittance spectra of the glass substrate with and without CS and A-CS nanocoatings recorded by UV–Vis spectrophotometry (a), reflectance curves of the bare substrate and the same coatings on silicone, measured by scanning-angle reflectometry (b), and the cross-section electron microscopic images of a CS (c) and an A-CS (d) coating on silicon substrate (scale bars are 300 and 200 nm long in images c and d, respectively, the area framed in green represents the enlarged details in image d). (For interpretation of the references to colour in this figure legend, the reader is referred to the Web version of this article.)

The thicknesses and refractive indices of the spin-coated layers on silicon substrate were investigated by scanning angle reflectometry. Fig. 3b shows the recorded reflectance curves for the bare Si substrate and for the coated samples. The fitting resulted in an average thickness of 118 ± 10 nm and refractive index of 1.534 ± 0.004 (n = 12) for the Si/CS samples and 140 ± 13 nm and 1.511 ± 0.015 (n = 12) for the Si/A-CS samples which means an average layer thickness increase of 19 ± 3 %.

The determined refractive index values from the two measurement techniques are in a good agreement for every coating, although the layer thicknesses are different for the dip- and for the spin-coated samples. During the acetylation reaction, side groups that require more space are incorporated into the material, which are also inhibit the formation of hydrogen bonds. This can lead to an increase in layer thickness [24]. Fig. 3c and d shows the cross-section electron microscopic images of a characterizing CS and A-CS coating. The layer thicknesses determined from the images (129 ± 4 nm for the CS and 150 ± 5 nm for the A-CS sample) are in a good agreement with (p < 0.05) that of calculated from the reflectance curves of the same samples (128 nm and 151 nm, respectively).

3.2.2. ATR-FTIR spectroscopy

The recorded infrared spectra of the CS and A-CS coatings on glass substrate are shown in Fig. 4, where the effect of the reaction on the chemical structure of the substance can be clearly observed. In the case of the A-CS coating, the peaks associated with the presence of the amide group (between 1250 and 1750 cm^{-1}) are much more intense and sharper. These are the Amide-I band (from the C═O streching vibration, around 1650 cm^{-1}, marked with long arrow) and the Amide-II band (from the N–H bendig vibration and C–N
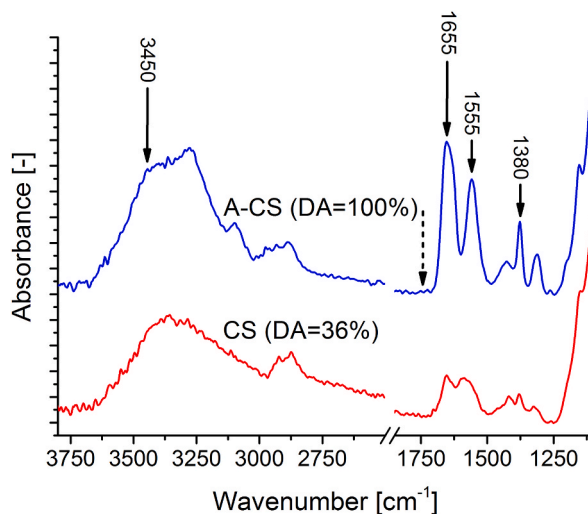
Fig. 4. ATR-FT-IR spectra of a CS and A-CS coating. The black arrows indicate peaks identifying chemical changes occurring during the acylation reaction (see text for detailed explanation).

streching vibration, around 1550 cm^{-1}, marked with short arrow). Between 1300 and 1400 cm^{-1} a complex multiple peak appears (the sharpest one is marked with another short arrow), which is called Amide-III band, and it is also from the previously mentioned streching and bendig [35]. The higher intensity of the peaks of the A-CS coating can be the result of the increase in layer thickness.

The spectra in Fig. 4 also prove that only *N*-acetylation occurs during the chemical modification. Since in the case of *O*-acetylation, the peak associated with the C=O streching vibration in the ester group is around *ca.* 1750 cm^{-1} [36], but there is no sign of a peak in this region in the spectrum of the A-CS coating (the absence is indicated by a dashed arrow). This significant decrease in the number of protonatable amino groups can lead to a less polar bulk phase, which also affects the swelling properties.

There is a wide peak between 3000 and 3500 cm^{-1}, which is associated with the O–H sterching vibration of the OH-groups of chitosan and the absorbed water molecules. Since only *N*-acylation happens during the reaction, the intensity of this peak is theoretically independent of the DA, while the intensity of the amide bands clearly depends on it. Eq. (1) uses this phenomenon to calculate the DA of the coating from the ratio of the intensities measured at the wavenumbers marked with long arrows. The results were 36 ± 3 % for the CS and 100 ± 3 % for the A-CS as shown in the figure. The increase in DA is significant (n = 12, p < 0.05).

3.2.3. Swelling studies

Fig. 5 summarises the results of the swelling studies, which were carried out using the scanning angle reflectometric method in a liquid chamber on CS and A-CS coatings deposited onto silicon substrate. Fig. 5a shows a typical measurement data set for the swelling of CS coating in BR buffer of pH 7.4. The reflectivity curve of the bare silicon substrate is also shown. In addition, the time evolution of the swelling degrees (the percentage increase in the volume of the layers) can be seen for all the investigated systems in Fig. 5b.
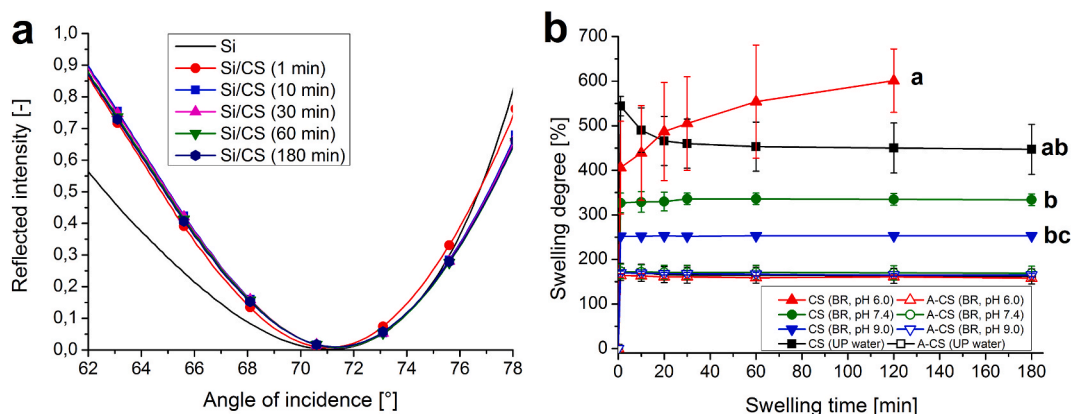

Fig. 5. Results of the swelling experiments. Reflectance curves of a bare silicone substrate and a Si/CS system in BR buffer solution of pH 7.4 (a), and the degrees of swelling in time for all the studied systems (b). The letters a-c at the end of the data lines indicate significant differences in the case of the CS samples, where the different letters mean significantly different data values (Mean $\pm$ standard deviation, n = 3, p < 0.05) (BR means Britton–Robinson buffer solution with a given pH, and UP water means ultrapure water).

3.2.3.1. Constrained swelling. The constrained swelling of the layer should be verified by proving that the coating does not move laterally during the swelling, and hence the change in the layer thickness properly characterizes the swelling process. To do this, the change in the distance of polystyrene nanoparticles mixed into the chitosan coating were investigated using dark field optical microscopy (similarly as Yoon et al. [22]). Fig. 6b and c shows the microscopic image of a coating before and after swelling it in pH 7.4 BR buffer solution. It can be seen from the images that the recordings were taken from the same area, so the distance of the same pair of particles could be determined. In the majority of cases (CS and A-CS coatings at different pHs), the increase in the distance between the particles was not significantly different from 0 ($p < 0.05$) and in all cases was below 0.5 %, which also confirms the constrained swelling. The detailed results can be found in Appendix A.

The above method gave a direct information about the constrained swelling. However, it is also possible to draw the same conclusion from the refractive index and thickness change of the swelling coatings. Considering the swollen polymer coating as a homogeneous medium, we can calculate the amount of theoretical water absorption based on the effective refractive index. If there is a case of constrained swelling, only the thickness of the coating increases during swelling, so it will be proportional to the water absorption. Therefore, a comparison of the theoretical thickness calculated from the effective refractive index and the measured thickness can confirm the phenomenon.

For this purpose, the Drude model (an effective medium approximation) was used, which is common to characterize swelling polymer gels as well as composit coatings [37,38]. It assumes, that the atomic constituents of the material are polarized by the externaly applied electric field only [39]. The relation for the model is given by:

$$n_{eff}^2 = (1 - \varphi)n_w^2 + \varphi n_p^2 \qquad (3)$$

where n_{eff} is the effective refractive index of the coating (in this case, the measured refractive index) and n_w is the refractive index of the water or buffer solution which was 1.332 and 1.334 respectively. n_p is the refractive index of the polymer (for this, the previously measured values for each dry coating was used), and φ is the volume fraction of the polymer in the gel. Assuming the case of constrained swelling φ can be calculated using the measured thicknesses before and after the swelling process, by the following equation.

$$\varphi = \frac{d_0}{d(t)} \qquad (4)$$

where d_0 is the thickness of the dry coating, and $d(t)$ is the thickness of the coating after a certain time of swelling. By substituting equation (4) into equation (3), the theoretical layer thickness of the swollen coatings can be calculated based on the measured refractive index. The calculated layer thickness can be compared with the measured value, as can be seen for a typical set of measurements (A-CS coating in BR buffer of pH 9.0) in Fig. 6c. It can be observed, that the measured and calculated values are sufficiently close to each other (the difference was under 10 % in all cases), which confirms that constrained swelling occurs due to strong interactions with the rigid substrate [40].

Due to the this phenomenon, the degree of swelling (*S*) of the coatings can also be calculated from the layer thicknesses measured in the dry (d_0) and swollen (*d*) state using the formula below (5).

$$S\,[\%] = \frac{d - d_0}{d_0} \bullet 100 \qquad (5)$$

3.2.3.2. The time evolution of swelling. The limitation (equilibrium) value of swelling degree can be reached in the first 30 min of swelling, with two exceptions. One is the case of CS coating in pH 6.0 buffer solution. Since chitosan dissolves below ca. pH 6.5 (its pKa value) due to the sufficiently high degree of protonation of the amino groups [41], in this case the high S and the large deviation in the results can be explained by the dissolution of the coating (Fig. 5b, filled red upright triangles). This is also confirmed by the fact that there was no visible coating on the substrate after the swelling measurement. The other exception is the case of the CS coating in ultrapure water, where S rapidly increases, then slowly decreases reaching its limitation value (ca. 450 %). This kind of "overswelling" effect has already been observed for similar chitosan-based systems [42,43]. In those cases, the phenomenon was explained by the
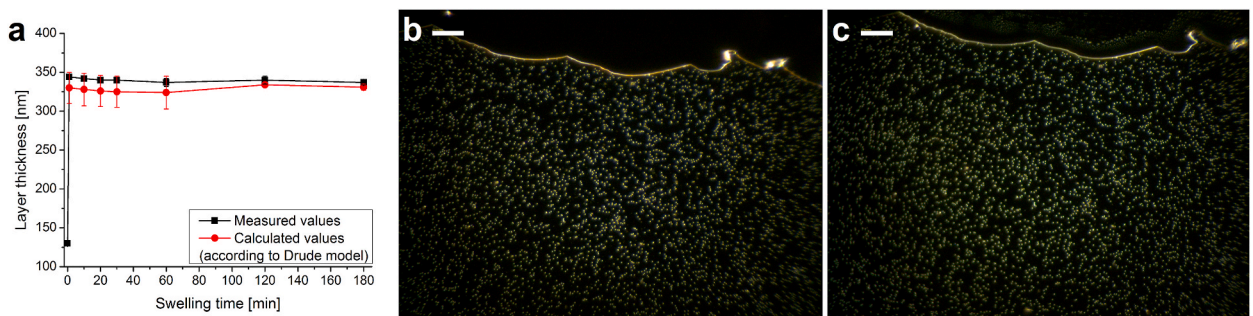

Fig. 6. Measured and calculated layer thickness values for a swollen A-CS coating in BR buffer of pH 9.0 (a) and dark field microscopic images of the same area of a CS coating before (b) and after (c) swelling the sample in pH 7.4 BR buffer solution (scale bars are 20 μm long in both images).

buffer salts or residual acetic acid (osmotic effects) [44]. In the precursor solution containing acetic acid, the polymer is fully protonated, and when the coatings dried, a lot of acetate ions were trapped among the polymer chains. This high counterion concentration initiates significant osmotic flow when the coating is placed in ultrapure water, but later the degree of protonation reaches the value corresponding to the pH of the water and the excess counterions diffuse out of the coating, reaching an equilibrium value.

3.2.3.3. pH-dependent swelling. Fig. 5b shows, that the swelling degree of A-CS samples is significantly lower than that of the CS coatings in every case. These values are below 200 %, while in the case of CS coatings they can reach 500–600 % depending on the pH of the aqueous solution. Although the osmotic flow does not cause "overswelling effect" in the case of the buffer solutions, it may also be responsible for the pH dependence of the swelling degrees of CS coatings: the limitation value of S is significantly increasing (n = 3, p < 0.05) with decreasing the pH (the pH of the ultrapure water is slightly acidic due to the possibly dissolved CO_2). As the pH of the swelling medium decreases, the degree of protonation of chitosan increases, which results in higher charge density, higher counterion concentration and therefore higher osmotic flow [45–47]. In addition, electrostatic repulsion occurs between the protonated amino groups, which further extends the coating [48]. A slight increase in the ionic strength of the buffer with increasing pH also amplifies the above mentioned effect [49,50]. In the case of the A-CS coatings there is no significant pH-dependence (n = 3, p < 0.05) due to the lacking of protonatable amino grops. This results in a small osmotic flow, minimal electrostatic repulsion and a much lower limitation value of S, which is compounded by the presumably higher crystallinity of the samples [34]. Katan an coworkers investigated the swelling of slightly thinner (ca. 30 nm) chitosan coatings using the quartz crystal microbalance technique. They also found that the degree of swelling of chitosan nanocoatings is strongly pH-dependent (especially in the acidic range), but almost no pH dependence was observed for acetylated coatings [51].

3.2.3.4. Comparison with contact angles. A comparison of wetting and swelling data reveals an interesting phenomenon. While the surface of the coatings became more polar as a result of the *N*-acetylation reaction (resulting in lower contact angles), the bulk phase became more apolar, as the equilibrium water absorption (degree of swelling) is lower. This means that the chemical reaction changed the polarity of the surface and bulk phase of the coatings in the opposite direction. This highlights the complexity of the system and shows that the previously mentioned reorganization of the functional groups can influence the surface properties almost independently
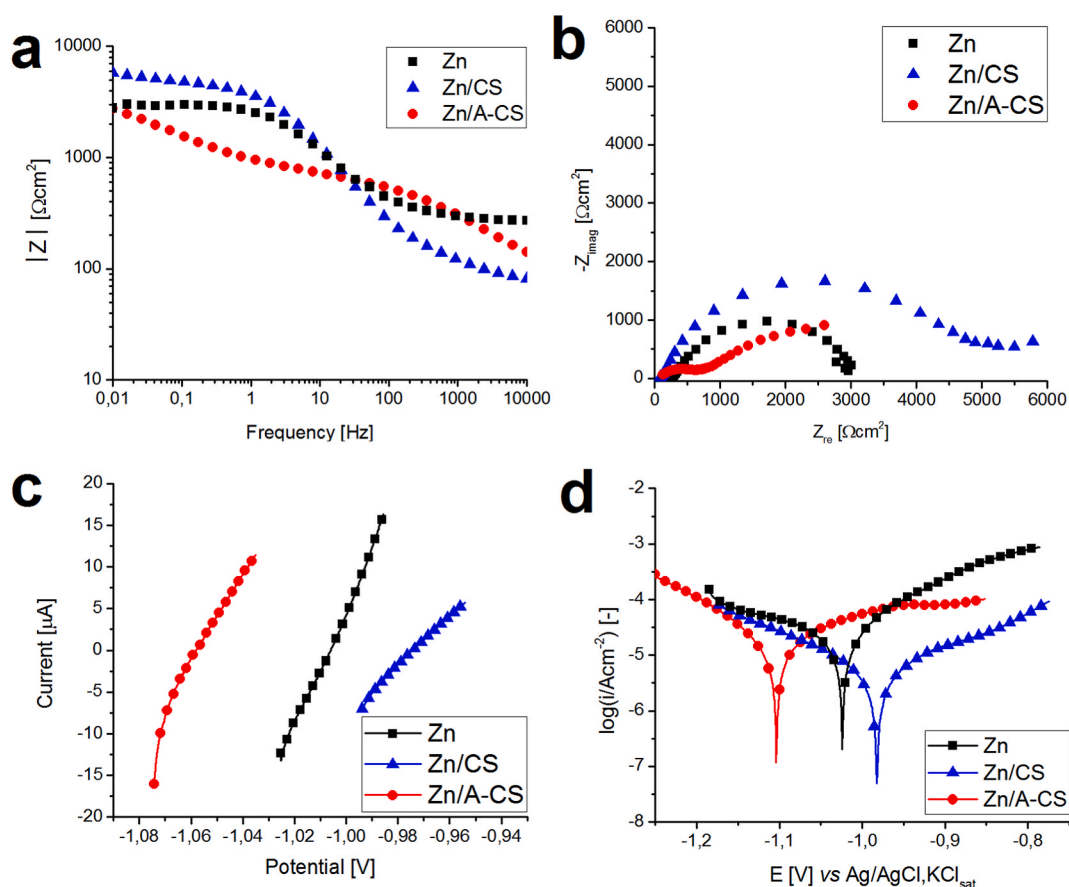

Fig. 7. Frequency dependence of absolute impedance |Z| (Bode)- (a) and Nyquist-plot (b) of the impedance spectra, the linear polarization- (c) and semi-logarithmic polarization-curves (d) of the bare and CS or A–CS–coated zinc substrate.

of the bulk phase.

However the swelling results are also consistent with the data in Table 1 summarizing the time evolution of the contact angles. The rapid decrease of the contact angle measured with a buffer of pH 6 in the case of the CS coating can be associated by the dissolution of the coating in the same case in the swelling measurements. In the case of the A-CS coating, neither the rapid decrease in the contact angle nor the dissolution was observed in the case of the same buffer solution, which means that although the pH-responsivity of the coating ceases as a result of acylation, its resistance to acidic media improves.

3.2.4. Electrochemical measurements

Electrochemical tests of a coated metal can provide information on the permeability of the thin layer. The corrosive species can reach the metal surface (in this case Zn) through the pores of the coating and consequently cause the oxidation (corrosion) of the metal. The first step of the measurements was the OCP determination, representing the resting potential and the basis for all other electrochemical tests. The shift to more positive values of the CS samples' OCP (Table 2.) suggest a less amount of electrolyte solution that reaches the metal surface through the coating. On the contrary, the negative shift of the A-CS samples' OCP can indicate, that the corroding electrolyte solution penetrates the layer and reaches the metal surface [52]. This observation regarding the coated samples has been confirmed by the results of the EIS measurements too. In Fig. 7a the variation of impedance modulus (|Z|) vs frequency is depicted, whose value at 0.01 Hz can be correlated with the coating's barrier properties. The absolute impedance value of the CS-coated sample (5,81 kΩcm^2) is larger than it is in the case of A-CS coating (2.75 kΩcm^2), therefore it can be concluded that the former provides better protection than the latter. The same trend can be observed in the complex plane representation of the impedance (Nyquist plots, Fig. 7b), where the largest loop belongs to the CS sample.

The linear (Fig. 7c) and semi-logarithmic (Fig. 7d) curves, were obtained as a result of the potentiodynamic polarization of the CS and A–CS–coated samples and the bare Zn. The Tafel interpretation of the polarization curves (Fig. 7d) provides information about the kinetic parameters like corrosion current densities and potential (i_{corr}, E_{corr}). They can be obtained from the intersection of the fitting lines to the two branches of the polarization curves and their incline is the anodic and cathodic Tafel slopes (b_a and b_c) (these values are introduced in Table 2.).

The corrosion current density (i_{corr}) reflect the oxidation rate of the metal due to the interaction with aggressive species reached its surface. The inhibition efficiency (*IE*) for the different samples was calculated with equation (6) and their values are also introduced in Table 2. In the equation i^o_{corr} represents the corrosion current density of the bare substrate and i_{corr} is the same quantity for the coated Zn. From the obtained results for IE, we can conclude that the barrier property of the A-CS is lower than that of the native chitosan indicating a more penetrable coating.

$$IE\ [\%] = \frac{i^o_{corr} - i_{corr}}{i^o_{corr}} \bullet 100 \tag{6}$$

The *pseudo-porosity* (*P*) of the CS and A-CS coatings can be calculated (see Table 2.) with formula (6), where the R_p and represents the polarization resistance of the coated metal and R_{ps} is the same quantity for the bare Zn. According to this model the electrolyte reaches the metal only through the pores of the coatings [53], therefore, it can be used for an approximate evaluation of the permeability (Eq. (7)) of the coatings [54–56]. The ΔE_{corr} is the difference of the Zn and coated substrate corrosion potentials determined from linear polarization measurements. The b_a (anodic Tafel slope of the Zn) was determined from semi-logarithmic polarization curves (Fig. 7d) [12].

$$P\ [\%] = \frac{Rp_s}{Rp} \bullet 10^{-|\Delta E_{corr}/b_a|} \bullet 100 \tag{7}$$

Finally, it can be concluded that both DC and AC electrochemical measurements results confirm the more permeable character of the A-CS nanolayers. This finding seems to contradict the fact that the *N*-acetylated coatings had a lower degree of swelling, since in general, hydrogels with a higher degree of swelling are more permeable [57,58]. However, it is well known that some of the water in swollen hydrogels is present in "bound" form (for example, it hydrates the protonated amino groups or the other polar groups in the sugar rings in the chitosan [59,60]). This bound water is non-freezable and its amount increases with the number of ionic groups in the hydrogel [61]. The linear polarization measurement calculates the *pseudo-porosity* of the layer based on ion transport, which can probably only be realized in channels consisting of "unbound" water so the *pseudo-porosity* does not actually correlate with the total amount of water in the swollen coating, but with the amount of free (unbound) water. From the degree of swelling and the *pseudo-porosity* values, it can be calculated that roughly 67.4 % of the total water content of native coatings is in bounded form, while this value is 50.8 % for *N*-acetylated coatings (for detailed calculations see Appendix B). This can probably be attributed to the more polar bulk phase of the coatings (also following from the swelling data).

4. Conclusions

The wetting and swelling behaviour of the initial (native) and fully *N*-acetylated chitosan nanocoatings were studied with Britton–Robinson buffer solutions of pH 6.0, 7.4 and 9.0. It was found that the surface of the coatings became more hydrophilic due to the chemical reaction. Contrarily, the swelling degree of the native coatings was significantly higher than that of their acetylated counterparts indicating the more hydrophilic character of the native coating matrix. The surprising contradiction between the bulk and the surface hydrophilicity in the case of the native coatings, was explained by the surface reorganization of the functional groups against

the non-polar air phase during the drying after the film deposition. Interestingly the matrix polarity manifested itself not only in the pH- dependence of the swelling but in the time evolution of water contact angles: pH-dependent deterioration of contact angles was only observed for the native coatings. Neither the swelling nor the wetting properties were significantly dependent on the pH in the case of the acetylated ones. Cationic permeation was found to be lower for the highly swelled (native) chitosan layers in electrochemical polarization measurements. This observation was explained in terms of the smaller amount of unbound water in the swelled native layers.

Funding

Data availability statement

Data related to the study, which are not included in the figures and tables or in the Appendix, are not available in public repositories, but can be made available on request.

CRediT authorship contribution statement

Péter Márton: Writing – review & editing, Writing – original draft, Visualization, Methodology, Investigation, Conceptualization. **Beáta Szolnoki:** Supervision, Methodology, Investigation. **Norbert Nagy:** Supervision, Methodology, Investigation. **András Deák:** Supervision, Methodology, Investigation. **Dániel Zámbó:** Supervision, Methodology, Investigation. **Gabriella Stefánia Szabó:** Writing – original draft, Validation, Methodology, Investigation, Conceptualization. **Zoltán Hórvölgyi:** Writing – review & editing, Writing – original draft, Validation, Supervision, Project administration, Conceptualization.

Declaration of competing interest

The authors declare that they have no known competing financial interests or personal relationships that could have appeared to influence the work reported in this paper.

Acknowledgments

Appendix A

Particle distance measurements before and after swelling.

1. Experimental

The phenomenon of constrained swelling was studied using a method similar to that used by Yoon et al. [1] 50 μL of a suspension containing of 5 % (w/w) polystyrene nanoparticles with a diameter of 315 nm was mixed with 30 ml of the 1 % chitosan solution with a Falc MIX20 test tube stirrer. A coating was formed from the solution onto glass substrates by dip-coating as described in section 2.2.1, and then some of the samples were *N*-acetylated as discussed in section 2.2.2. The dried layers were scratched, and based on the scratch, microscopic images were taken of a certain area with an Olympus BX51 instrument at different magnifications and in bright and dark field modes. After 10 min of swelling in BR buffer solutions of pH 6.0, 7.4 and 9.0, the excess liquid was quickly blown off the samples with N_2 gas, and then, based on the scratches, microscopic images were taken of the same areas as before swelling. To study the lateral movement of the particles, the distance between selected pairs of particles in the dark field images before and after swelling were measured. Five distances were measured in the vertical and five in the horizontal direction on the images. To investigate the lateral movement due to the acetylation reaction, the average density of the particles in the images before swelling were determined for three replicate CS and ACS samples. The measurements were carried out with ImageJ software [2].

2. Results

The microscopic images and the measured distances of a CS coating are presented in Fig. A1. Fig. A1a and A1d shows the same area of the coating before and after swelling it in pH 7.4 BR buffer. The slight blurring of the particles and the liquid drops visible at the top of the image prove that the coating was wet and in a swollen state. The lines on the images are the measured distances between the selected pairs of particles.
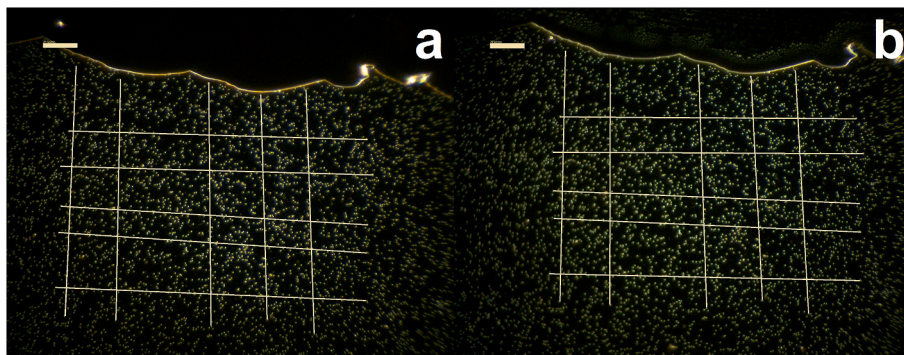
Fig. A1. Dark field images of a CS coating in dry (a) and swollen (b) state (pH = 7.4, same images as on Fig. 6b and c). The lines are the measured distances between 10 pairs of particles (scale bars are 20 μm long in both images).

The distance of ten chosen pair of particles were measured in the dark field images before and after swelling (five measurement in the horizontal and five in the vertical direction) in the case of CS and A-CS samples and all buffer solutions. The relative change in the distance of the particles were calculated with equation (6).

$$\Delta l_{rel} \; [\%] = \frac{l - l_0}{l_0} \bullet 100 \tag{A1}$$

where l_0 and l are the distances of a chosen pair before and after swelling. The Δl_{rel} values are summarized in Table A1 in the different directions and in total. Since the thickness of the layer increased as a result of the acetylation reaction (see section 3.2.1), the density of the particles (number of particles on a μm^2) was also measured on the CS and ACS coatings before swelling, to find out whether this increase in thickness also a constrained volume increase.

One can see from Table A1, that the relative increase in the particle distance is not significantly different from zero except for two cases (n = 5, p < 0.05), and in all cases it is negligibly small compared to the previously measured increases in layer thickness (see section 3.2.3). This observation confirms that for the investigated coatings, constrained swelling takes place. The particle density values do not differ significantly in the case of the CS and A-CS samples (n = 3, p < 0.05), which allows us to conclude that not only the swelling, but also the volume increase during the acetylation reaction takes place in one dimension.

Table A1
Results of the distance and particle density measurements on the dark field microscopic images of the samples before and after swelling (Mean ± standard deviation). The Δl_{rel} values marked with an asterisk are significantly different from zero (n = 5 or 10, p < 0.05).

Sample	pH [−]	Δl_{rel} [%]			Particle density [1/μm^2]
		Horizontal	Vertical	Overall	
Glass/CS	6.0	0.1 ± 0.3	0.1 ± 0.1	0.1 ± 0.2	0.1 ± 0.01
	7.4	−0.1 ± 0.4	−0.4 ± 0.1*	−0.2 ± 0.3*	
	9.0	0.1 ± 0.1	0.0 ± 0.2	0.0 ± 0.2	
Glass/A-CS	6.0	0.1 ± 0.2	0.5 ± 0.4*	0.3 ± 0.4*	0.1 ± 0.00
	7.4	−0.1 ± 0.4	0.4 ± 0.4	0.2 ± 0.5	
	9.0	−0.2 ± 0.2	0.0 ± 0.3	−0.1 ± 0.3	

Appendix B

Calculation the ratio of bounded water in the hydrogel based on linear polarization measurements.
The degree of swelling were defined in equation (5) as follows:

$$S \; [\%] = \frac{d - d_0}{d_0} \bullet 100 \tag{B1}$$

where d_0 and d are the thicknesses of the dry and swollen coating respectively. The water content (W) of the hydrogel can be defined with the same notations as:

$$W \; [\%] = \frac{d - d_0}{d} \bullet 100 \tag{B2}$$

From equation (B1) and B2, W can be expressed as a function of S:

$$W = \frac{S}{100 + S} \tag{B3}$$

It can be assumed, that the pseudo-porosity (P) of the swollen sample is equal to the unbound water content of the hydrogel. From P and W, the unbounded ratio of the water content can be expressed as follows:

$$W_{unb}[\%] = \frac{P}{W} \bullet 100 \tag{B4}$$

Finally, the ratio of the water in bounded form is 100-W_{unb}.

References

[1] I. Aranaz, R. Alc, M. Concepci, Chitosan : an Overview of its properties and applications, Polymers 13 (2021) 3256.

[2] M. Islam, S. Biswas, N. Sakib, T. Ur, Bioactive Materials Chitosan based bioactive materials in tissue engineering applications-A review, Bioact. Mater. 5 (2020) 164–183, https://doi.org/10.1016/j.bioactmat.2020.01.012.

[3] Z. Sebestyén, E. Jakab, A. Domán, P. Bokrossy, I. Bertóti, J. Madarász, K. László, Thermal degradation of crab shell biomass, a nitrogen-containing carbon precursor, J. Therm. Anal. Calorim. (2020), https://doi.org/10.1007/s10973-020-09438-9.

[4] J. Wattjes, S. Sreekumar, C. Richter, S. Cord-landwehr, R. Singh, N. Eddine, E. Gueddari, B.M. Moerschbacher, Patterns matter part 1 : chitosan polymers with non-random patterns of, React. Funct. Polym. 151 (2020), 104583, https://doi.org/10.1016/j.reactfunctpolym.2020.104583.

[5] E. Rostami, Progresses in targeted drug delivery systems using chitosan nanoparticles in cancer therapy : a mini-review, J. Drug Deliv. Sci. Technol. 58 (2020), 101813, https://doi.org/10.1016/j.jddst.2020.101813.

[6] Á.F. Szőke, G.S. Szabó, Z. Hórvölgyi, E. Albert, L. Gaina, L.M. Muresan, Eco-friendly indigo carmine-loaded chitosan coatings for improved anti-corrosion protection of zinc substrates, Carbohydr. Polym. 215 (2019) 63–72, https://doi.org/10.1016/j.carbpol.2019.03.077.

[7] Á.F. Szőke, G.S. Szabó, Z. Hórvölgyi, E. Albert, A.G. Végh, L. Zimányi, L.M. Muresan, Accumulation of 2-Acetylamino-5-mercapto-1,3,4-thiadiazole in chitosan coatings for improved anticorrosive effect on zinc, Int. J. Biol. Macromol. 142 (2020) 423–431, https://doi.org/10.1016/j.ijbiomac.2019.09.114.

[8] P. Pal, A. Pal, K. Nakashima, B. Kumar, Chemosphere Applications of chitosan in environmental remediation : a review, Chemosphere 266 (2021), 128934, https://doi.org/10.1016/j.chemosphere.2020.128934.

[9] A. Spoiala, C.-I. Ilie, D. Ficai, A. Ficai, Chitosan-based nanocomposite polymeric membranes for water purification — a review, Materials 14 (2021) 1–29.

[10] B. Gyarmati, G. Stankovits, B.Á. Szilágyi, D.L. Galata, P. Gordon, A. Szilágyi, A robust mucin-containing poly (vinyl alcohol) hydrogel model for the in vitro characterization of mucoadhesion of solid dosage forms, Colloids Surf., B 213 (2022), 112406, https://doi.org/10.1016/j.colsurfb.2022.112406.

[11] F. Goycoolea, A. Heras, I. Aranaz, G. Gemma, M. Fernández-Valle, W. Argüelles-Monal, Effect of chemical crosslinking on the swelling and shrinking properties of thermal and pH-responsive chitosan hydrogels, Macromol. Biosci. 3 (2003) 612–619, https://doi.org/10.1002/mabi.200300011.

[12] P.D. Lairenjam, S.K. Sukumaran, D.K. Satapathy, Modulation of optical anisotropy in chitosan thin films: role of swelling, Macromolecules 54 (2021) 10931–10942, https://doi.org/10.1021/acs.macromol.1c00613.

[13] M. Dabóczi, E. Albert, E. Agócs, M. Kabai-Faix, Z. Hórvölgyi, Bilayered (silica-chitosan) coatings for studying dye release in aqueous media: the role of chitosan properties, Carbohydr. Polym 136 (2016) 137–145, https://doi.org/10.1016/j.carbpol.2015.09.025.

[14] H. Lee, D.M. Eckmann, D. Lee, N.J. Hickok, R.J. Composto, Symmetric pH-dependent swelling and antibacterial properties of chitosan brushes, Langmuir 27 (2011) 12458–12465.

[15] J.M. Chem, H. Lee, M.Q. Yee, Y.Y. Eckmann, N.J. Hickok, M. Eckmann, R.J. Composto, Reversible swelling of chitosan and quaternary ammonium modified chitosan brush layers : effects of pH and counter anion size and functionality, J. Mater. Chem. 22 (2012) 19605–19616, https://doi.org/10.1039/c2jm34316a.

[16] P. Márton, Ö.T. Nagy, D. Kovács, B. Szolnoki, J. Madarász, N. Nagy, G.S. Szabó, Z. Hórvölgyi, Barrier behaviour of partially N -acetylated chitosan layers in aqueous media, Int. J. Biol. Macromol. 232 (2023), 123336, https://doi.org/10.1016/j.ijbiomac.2023.123336.

[17] I. Mohammed-Ziegler, I. Tánczos, Z. Hórvölgyi, B. Ágoston, Water-repellent acylated and silylated wood samples and their surface analytical characterization, Colloids Surfaces A Physicochem. Eng. Asp. 319 (2008) 204–212, https://doi.org/10.1016/j.colsurfa.2007.06.063.

[18] G. Ladam, P. Schaad, J.C. Voegel, P. Schaaf, G. Decher, Ä. Europe, in situ determination of the structural properties of initially deposited polyelectrolyte multilayers, Langmuir 16 (2000) 1249–1255.

[19] A. Deák, E. Hild, A.L. Kovács, Z. Hórvölgyi, Contact angle determination of nanoparticles: film balance and scanning angle reflectometry studies, Phys. Chem. Chem. Phys. 9 (2007) 6359–6370, https://doi.org/10.1039/b702937n.

[20] A. Agod, A. Deák, E. Hild, Z. Hórvölgyi, E. Kálmán, G. Tolnai, A.L. Kovács, Contact angle determination of nanoparticles: real experiments and computer simulations, J. Adhes. 80 (2004) 1055–1072, https://doi.org/10.1080/00218460490509381.

[21] R. Marcombe, S. Cai, W. Hong, X. Zhao, Y. Lapusta, Z. Suo, A theory of constrained swelling of a pH-sensitive hydrogel, Soft Matter 6 (2010) 784–793, https://doi.org/10.1039/b917211l.

[22] J. Yoon, S. Cai, Z. Suo, R.C. Hayward, Poroelastic swelling kinetics of thin hydrogel layers: comparison of theory and experiment, Soft Matter 6 (2010) 6004–6012, https://doi.org/10.1039/c0sm00434k.

[23] J. Yoon, S. Cai, R.C. Hayward, Poroelastic swelling kinetics of thin hydrogel layers : comparison of theory and experiment, Soft Matter 6 (2010) 6004–6012, https://doi.org/10.1039/c0sm00434k.

[24] P. Márton, E. Albert, N. Nagy, B. Tegze, G.S. Szabó, Z. Hórvölgyi, Chemically modified chitosan coatings: wetting and electrochemical studies, Stud. Univ. Babes-Bolyai, Chem. 65 (2020) 63–79, https://doi.org/10.24193/subbchem.2020.3.05.

[25] C.Y. Choi, S.B. Kim, P.K. Pak, D. Il Yoo, Y.S. Chung, Effect of N-acylation on structure and properties of chitosan fibers, Carbohydr. Polym. 68 (2007) 122–127, https://doi.org/10.1016/j.carbpol.2006.07.018.

[26] Index @ Gwyddion.Net, (n.d.). http://gwyddion.net/.

[27] Z. Cui, E.S. Beach, P.T. Anastas, Modification of chitosan films with environmentally benign reagents for increased water resistance, Green Chem. Lett. Rev. 4 (2011) 35–40, https://doi.org/10.1080/17518253.2010.500621.

[28] A. Deák, E. Hild, A.L. Kovács, Z. Hórvölgyi, Characterisation of solid supported nanostructured thin films by scanning angle reflectometry and UV-vis spectrometry, Mater. Sci. Forum 537–538 (2007) 329–336. https://doi.org/10.4028/www.scientific.net/msf.537-538.329.

[29] J. Domszy, G. Roberts, Evaluation of infrared spectroscopic techniques for analysing chitosan, Die Makromol. Chemie. 186 (1985) 1671–1677, https://doi.org/10.1002/macp.1985.021860815.

[30] E. Hild, T. Seszták, D. Völgyes, Z. Hórvölgyi, Characterisation of Silica Nanoparticulate Layers with Scanning-Angle Reflectometry, 2004, pp. 61–67.

[31] C.A. Schneider, W.S. Rasband, K.W. Eliceiri, HISTORICAL commentary NIH Image to ImageJ : 25 years of image analysis, Nat. Methods 9 (2012) 671–675, https://doi.org/10.1038/nmeth.2089.

[32] Á.F. Szőke, G. Szabó, Z. Simó, Z. Hórvölgyi, E. Albert, A.G. Végh, L. Zimányi, L.M. Muresan, Chitosan coatings ionically cross-linked with ammonium paratungstate as anticorrosive coatings for zinc, Eur. Polym. J. 118 (2019) 205–212, https://doi.org/10.1016/j.eurpolymj.2019.05.057.

[33] M.A. Hubbe, What is the real value of chitosan's surface energy? Biomacromolecules 9 (2008) 610–614, https://doi.org/10.1021/bm701199g.

[34] E.F. Franca, L.C.G. Freitas, R.D. Lins, Chitosan molecular structure as a function of N-acetylation, Biopolymers 95 (2011) 448–460, https://doi.org/10.1002/bip.21602.

[35] E. Atangana, T.T. Chiweshe, H. Roberts, Modification of novel chitosan-starch cross-linked derivatives polymers: synthesis and characterization, J. Polym. Environ. 27 (2019) 979–995, https://doi.org/10.1007/s10924-019-01407-0.

[36] L. Liu, S. Zhou, B. Wang, F. Xu, R. Sun, Homogeneous acetylation of chitosan in ionic liquids, J. Appl. Polym. Sci. 129 (2013) 28–35, https://doi.org/10.1002/app.38701.

[37] A. Murali, M. Ganesan, D.K. Satapathy, P.B.S. Kumar, Penetrant-induced glass-like transition in thin chitosan films, J. Phys. Chem. B 125 (2021) 12617–12626, https://doi.org/10.1021/acs.jpcb.1c07903.

[38] S. Kermadi, N. Agoudjil, S. Sali, M. Boumaour, S. Bourgeois, M.C. Marco De Lucas, Sol-gel synthesis of xTiO2(100 - X)SiO2 nanocomposite thin films: structure, optical and antireflection properties, Thin Solid Films 564 (2014) 170–178, https://doi.org/10.1016/j.tsf.2014.05.068.

[39] A. Feldman, Modeling refractive index in mixed component systems, Model. Opt. Thin Film. 821 (1987).

[40] H. Yan, B. Jin, Equilibrium swelling of a polyampholytic pH-sensitive hydrogel, Eur. Phys. J. E. 36 (2013) 1–7, https://doi.org/10.1140/epje/i2013-13027-x.

[41] K. Lavanya, S.V. Chandran, K. Balagangadharan, N. Selvamurugan, Materials Science & Engineering C Temperature- and pH-responsive chitosan-based injectable hydrogels for bone tissue engineering, Mater. Sci. Eng. C. 111 (2020), 110862, https://doi.org/10.1016/j.msec.2020.110862.

[42] D.P. Saldanha, M.V.M. Navarro, A.C. Medeiros, E.P. Azevedo, M.F. Ginani, F.N. Raffin, Mechanical properties and release studies of chitosan films impregnated with silver sulfadiazine, J. Appl. Polym. Sci. 102 (2006) 3462–3470, https://doi.org/10.1002/app.24537.

[43] T.T. Nge, N. Hori, A. Takemura, H. Ono, Swelling behavior of chitosan/poly(acrylic acid) complex, J. Appl. Polym. Sci. (2004) 2930–2940.

[44] D. Baskar, T.S.S. Kumar, Effect of deacetylation time on the preparation , properties and swelling behavior of chitosan films, Carbohydr. Polym. 78 (2009) 767–772, https://doi.org/10.1016/j.carbpol.2009.06.013.

[45] F.M. Goycoolea, M. Fernández-Valle, I. Aranaz, A. Heras, pH- and temperature-sensitive chitosan hydrogels : swelling and MRI studies, Macromol. Chem. Phys. 212 (2011) 887–895, https://doi.org/10.1002/macp.201000301.

[46] M. Omrani, M.R. Naimi-jamal, B.F. Far, The design of multi-responsive nanohydrogel networks of chitosan for controlled drug delivery, Carbohydr. Polym. 298 (2022), 120143, https://doi.org/10.1016/j.carbpol.2022.120143.

[47] J. Ostrowska-czubenko, M. Gierszewska, M. Pieróg, pH-responsive hydrogel membranes based on modified chitosan : water transport and kinetics of swelling, J. Polym. Res. 22 (2015) 153, https://doi.org/10.1007/s10965-015-0786-3.

[48] S.J. Kim, S. Yoon, I.Y. Kim, S.I. Kim, Swelling characterization of the semiinterpenetrating polymer network hydrogels composed of chitosan and poly (diallyldimethylammonium chloride), J. Appl. Polym. Sci. 91 (2004) 2876–2880.

[49] C. Mongay, V. Cerdrá, A Britton-Robinson buffer of known ionic strength, Ann. Chim. 64 (1974) 409–412.

[50] A. Singh, S.S. Narvi, P.K. Dutta, N.D. Pandey, External stimuli response on a novel chitosan hydrogel crosslinked with formaldehyde, Bull. Mater. Sci. 29 (2006) 233–238, https://doi.org/10.1007/BF02706490.

[51] T. Katan, R. Kargl, T. Mohan, T. Steindorfer, M. Mozetic, J. Kovac, K. Kleinschek, Solid phase peptide synthesis on chitosan thin films, Biomacromolecules 23 (2022) 731–742.

[52] R. Moaref, M.H. Shahini, H. Eivaz Mohammadloo, B. Ramezanzadeh, S. Yazdani, Application of sustainable polymers for reinforcing bio-corrosion protection of magnesium implants–a review, Sustain. Chem. Pharm. 29 (2022), 100780, https://doi.org/10.1016/j.scp.2022.100780.

[53] S. Feliu, J.M. Bastidas, J.C. Galvan, J. Simancas, M. Morcillo, E. Almeida, Electrochemical determination of rusted steel surface stability, J. Appl. Electrochem. 23 (1993) 157–161, https://doi.org/10.1007/BF00246953.

[54] R.B. Figueira, C.J.R. Silva, E.V. Pereira, Hybrid sol–gel coatings for corrosion protection of galvanized steel in simulated concrete pore solution, J. Coatings Technol. Res. 13 (2016) 355–373, https://doi.org/10.1007/s11998-015-9751-7.

[55] G.A. Phalak, D.M. Patil, S.T. Mhaske, Synthesis and characterization of thermally curable guaiacol based poly(benzoxazine-urethane) coating for corrosion protection on mild steel, Eur. Polym. J. 88 (2017) 93–108, https://doi.org/10.1016/j.eurpolymj.2016.12.030.

[56] S. Rastegari, E. Salahinejad, Surface modification of Ti-6Al-4V alloy for osseointegration by alkaline treatment and chitosan-matrix glass-reinforced nanocomposite coating, Carbohydr. Polym. 205 (2019) 302–311, https://doi.org/10.1016/j.carbpol.2018.10.082.

[57] R. Safdar, A.A. Omar, A. Arunagiri, I. Regupathi, M. Thanabalan, Potential of Chitosan and its derivatives for controlled drug release applications – a review, J. Drug Deliv. Sci. Technol. 49 (2019) 642–659, https://doi.org/10.1016/j.jddst.2018.10.020.

[58] Y. Herdiana, N. Wathoni, S. Shamsuddin, M. Muchtaridi, Drug release study of the chitosan-based nanoparticles, Heliyon 8 (2022), e08674, https://doi.org/10.1016/j.heliyon.2021.e08674.

[59] M. Yu, K. Zhang, X. Guo, L. Qian, Effects of the degree of deacetylation on the single-molecule mechanics of chitosans, J. Phys. Chem. B 127 (2023) 4261–4267, https://doi.org/10.1021/acs.jpcb.3c01661.

[60] M.N. Khalid, F. Agnely, N. Yagoubi, J.L. Grossiord, G. Couarraze, Water state characterization , swelling behavior , thermal and mechanical properties of chitosan based networks, Eur. J. Pharm. Sci. 15 (2002) 425–432.

[61] M. Gierszewska, J. Ostrowska-Czubenko, Chitosan-based membranes with different ionic crosslinking density for pharmaceutical and industrial applications, Carbohydr. Polym. 153 (2016) 501–511, https://doi.org/10.1016/j.carbpol.2016.07.126.

References

[1] J. Yoon, S. Cai, Z. Suo, R.C. Hayward, Poroelastic swelling kinetics of thin hydrogel layers: comparison of theory and experiment, Soft Matter 6 (2010) 6004–6012, https://doi.org/10.1039/c0sm00434k.

[2] C.A. Schneider, W.S. Rasband, K.W. Eliceiri, HISTORICAL commentary NIH Image to ImageJ : 25 years of image analysis, Nat. Methods 9 (2012) 671–675, https://doi.org/10.1038/nmeth.2089.